

Deep learning of stochastic contagion dynamics on complex networks

Charles Murphy, Edward Laurence, and Antoine Allard

Département de Physique, de Génie Physique, et d'Optique,

Université Laval, Québec (Québec), Canada G1V 0A6 and

Centre interdisciplinaire en modélisation mathématique,

Université Laval, Québec (Québec), Canada G1V 0A6

(Dated: February 1, 2022)

Forecasting the evolution of contagion dynamics is still an open problem to which mechanistic models only offer a partial answer. To remain mathematically and/or computationally tractable, these models must rely on simplifying assumptions, thereby limiting the quantitative accuracy of their predictions and the complexity of the dynamics they can model. Here, we propose a complementary approach based on deep learning where the effective local mechanisms governing a dynamic are learned automatically from time series data. Our graph neural network architecture makes very few assumptions about the dynamics, and we demonstrate its accuracy using stochastic contagion dynamics of increasing complexity on static and temporal networks. By allowing simulations on arbitrary network structures, our approach makes it possible to explore the properties of the learned dynamics beyond the training data. Our results demonstrate how deep learning offers a new and complementary perspective to build effective models of contagion dynamics on networks.

Our capacity to prevent or contain outbreaks of infectious diseases is directly linked to our ability to accurately model contagion dynamics. Since the seminal work of Kermack and McKendrick almost a century ago [1], a variety of models incorporating ever more sophisticated contagion mechanisms have been proposed, studied and used [2–5]. These mechanistic models have provided invaluable insights about how infectious diseases spread, and have thereby contributed to the design of better public health policies. However, several challenges remain unresolved, which call for contributions from new modeling approaches [6–8].

For instance, many complex contagion processes involve the nontrivial interaction of several pathogens [9–12], and some social contagion phenomena, like the spread of misinformation, require to go beyond pairwise interactions between individuals [13–15]. Also, while qualitatively informative, the forecasts of most mechanistic models lack quantitative accuracy. Indeed, most models are constructed from a handful of mechanisms which can hardly reproduce the intricacies of real complex contagion dynamics. One approach to these challenges is to complexify the models by adding more detailed and refined mechanisms. However, mechanistic models become rapidly intractable as new mechanisms are added. Moreover, more complex models require the specification of a larger number of parameters whose values can be difficult to infer from limited data.

On another front, the range of applications of deep learning has grown remarkably fast in recent years [16], from computer vision [17] to natural language processing [18] and time series forecasting [19]. More specifically, deep learning is now being applied to problems related to Network Science using tools like Graph Neural Networks (GNN) which have been designed to handle arbitrarily structured data [20–22]. Recent work showed great promise for applications in community detection and link prediction [23, 24], in the prediction of dynamical observables [25], in network reconstruction [26] and the detection of structural perturbations [27], as well as in the context of discovering new materials and drugs [28, 29]. In general, GNNs have been shown to adequately handle in-

tricate tasks, making them prime candidates to tackle several challenges of contagion dynamics modeling.

Here, we demonstrate how deep learning can be used to build effective models of stochastic contagion dynamics taking place on complex networks. Instead of constructing a model by specifying the mechanisms driving the dynamics, we consider learning these mechanisms directly from data. We start by posing the machine learning problem explicitly and propose a deep GNN architecture with a reliable protocol to train it. We demonstrate the validity of our approach using various dynamics on networks with increasing complexity on static and temporal networks. Finally, we show how our approach can provide predictions for previously unseen network structures, therefore allowing the exploration of the properties of the learned dynamics beyond the training data.

Our approach assumes that a hidden stochastic contagion dynamics takes place on a network $G = (\mathcal{V}, \mathcal{E})$, where \mathcal{V} is the set of nodes and \mathcal{E} is the set of links. As this hidden dynamical process evolves over time, it generates a multivariate time series $X = (X(t) : t \in [0, T])$, where $X(t)$ is the global state of the system at time t . This global state $X(t) = (x_i(t) : i \in \mathcal{V})$ consists of the state of every node i at this time, noted $x_i(t)$. We also denote the finite set of the possible node states by Ω , such that $x_i(t) \in \Omega$. We assume that this dynamical process can be entirely defined by its *local transition probabilities* (LTPs), denoted $p_{\sigma}^{\mu \rightarrow \nu}$. These correspond to the probability that a node of degree k in state μ at time t transitions to state ν at time $t + \Delta t$ given the states of its first neighbors σ , where $\mu, \nu \in \Omega$ and $\sigma \in \Omega^k$. By doing so, we assume that the hidden process is stationary, Markovian and discrete both in time and in terms of its available global states. Note that generalizing our approach to non-Markovian and/or continuous-state dynamics is straightforward; we choose to limit the presentation of our approach to these more restricting assumptions for the sake of clarity and conciseness.

We consider a trainable GNN model composed of a set of free and tunable parameters Θ that takes as inputs the current global state of the system, $X(t)$, and the structure of the

network at time t (e.g. its adjacency list), and outputs the predicted LTPs, denoted $\hat{p}_{\sigma}^{\mu \rightarrow \nu}(\Theta)$. Our objective is then to learn a set of parameters Θ^* such that

$$\hat{p}_{\sigma}^{\mu \rightarrow \nu}(\Theta^*) \approx p_{\sigma}^{\mu \rightarrow \nu}, \quad (1)$$

for all transitions $\mu, \nu \in \Omega$ and all possible neighborhoods σ . Note that there exist other techniques that can also perform this task. For instance, Bayesian approaches have been used for the parameters inference of simple and complex contagion under the assumption of a predefined model [30, 31]. In general, these approaches work well on synthetic data generated by the predefined model, in some cases even without the need of likelihood computations [31]. However, these simple models are only coarse representations of real systems. A more general approach is then to infer the complete Markov chains directly [32], where each LTP is considered as a parameter of the model. We adopt a similar strategy in that we use GNNs to parametrize these Markov chains with an underlying network structure. With their easily adaptable architecture, GNNs have the advantage of combining their parameters hierarchically to compute the LTPs as well as being universal estimators [33, 34], meaning that they can in principle estimate any set of LTPs. Furthermore, their parameters estimation is scalable and efficiently performed with stochastic gradient descent [35, 36].

In practice, the objective described by Eq. (1) must be encoded into a loss function, denoted $\mathcal{L}(\Theta)$. An appropriate choice is

$$\mathcal{L}(\Theta) = \sum_{k \in \mathcal{K}} \sum_{\mu \in \Omega} \sum_{\sigma \in \Omega^k} \frac{1}{Z} \left[- \sum_{\nu \in \Omega} p_{\sigma}^{\mu \rightarrow \nu} \log \hat{p}_{\sigma}^{\mu \rightarrow \nu} \right] \quad (2)$$

where \mathcal{K} is the set of degree classes, Z is the total number of possible input configurations (μ, σ) , and the term between brackets corresponds to the cross entropy between the LTPs of the underlying process (the “ground truth”) and the LTPs predicted by the GNN, $\hat{p}_{\sigma}^{\mu \rightarrow \nu}$. Equation (2) quantifies the information difference [37] between the original LTPs and the ones predicted by the GNN, averaged over a uniform distribution of all possible inputs (μ, σ) .

Two obstacles prevent the exact evaluation of Eq. (2) in realistic settings. First, the LTPs $p_{\sigma}^{\mu \rightarrow \nu}$ that we want the model to predict—the “ground truth”—are a priori unknown. Second, finite datasets only explore a finite fraction of the configuration space. We propose to resolve both of these issues by approximating Eq. (2) from the dataset X directly. To do so, we consider the following approximate loss,

$$\mathcal{L}(\Theta) \simeq \sum_{t \in \mathcal{T}'} \sum_{i \in \mathcal{V}'(t)} \frac{\omega_i(t)}{|\mathcal{T}'| |\mathcal{V}'(t)|} \left[- \log \hat{p}_{x_{\mathcal{N}_i}(t)}^{x_i(t) \rightarrow x_i(t+\Delta t)} \right], \quad (3)$$

where $\omega_i(t)$ is a weight assigned to node i at time t , $x_{\mathcal{N}_i}(t)$ is the state of the neighbors of node i at time t , and where $\mathcal{V}' \subseteq \mathcal{V}$ and $\mathcal{T}' \subseteq [0, T]$ are subsets of the training dataset. Note that the complements of these subsets can also be used to validate the model during training (see Supplementary Material).

Two approximations are at play in Eq. (3). First, the first three sums of Eq. (2) are approximated using a sampling

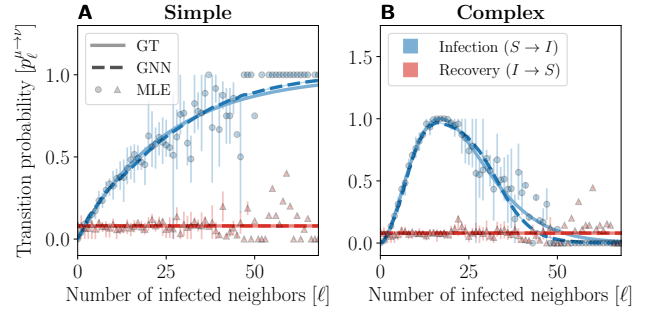


FIG. 1. (color online) **Validation of the predictions of GNNs trained on a Barabási-Albert random network (BA) [38] for the (A) simple and (B) complex contagion dynamics.** The solid lines correspond to the LTPs of the dynamics used to generate the training data (labeled GT for “ground truth”), and the dashed lines show the predictions of the GNNs. Markers correspond to the maximum likelihood estimation (MLE) of the LTPs computed from the training dataset. LTPs corresponding to transmission events are shown in blue ($S \rightarrow I$), and the ones related to recovery events are shown in red ($I \rightarrow S$). Lines and markers were obtained by averaging the LTPs over every σ corresponding to a same value of ℓ . The standard deviation around these average values is shown using a colored area around the lines (typically narrower than the width of the lines) and using vertical bars for the markers. The training datasets were generated using a BA network composed of $|\mathcal{V}| = 1000$ nodes and with average degree $\langle k \rangle = 4$, and we used the parameters $(\tau, \gamma) = (0.04, 0.08)$ and $(\eta, \gamma) = (8, 0.06)$ for the simple and complex contagion dynamics, respectively. All technical details related to training are provided in Supplementary Material.

scheme where the weights $\omega_i(t)$ rebalance the importance to “overrepresented” inputs, i.e. inputs (μ, σ) whose frequency of occurrence in X , noted $\rho(\mu, \sigma)$, is high. Choosing $\omega_i(t) = \rho(x_i(t), x_{\mathcal{N}_i}(t))^{-\lambda}$ effectively evaluates Eq. (3) with a relaxed version of importance sampling [39], which reduces the importance of frequent inputs and increases that of the rare ones. This procedure is identical to standard importance sampling when $\lambda = 1$. Second, the average over ν is replaced by a Monte Carlo approximation since the “ground truth” LTPs, $p_{\sigma}^{\mu \rightarrow \nu}$, are a priori unknown. Note that, for any specific input (μ, σ) , this approximation converges to its expected value only if the corresponding number of transitions found in the subsets of the training dataset is sufficiently large. This second approximation will therefore be necessarily poor for rare inputs, and we set $\lambda < 1$ to limit their influence on the quality of the training. To isolate the effect of this second approximation, we consider a *semi-exact* training scheme where only the first three sums of Eq. (2) are approximated using the importance sampling scheme, and the sum on ν is computed using the “ground truth” LTPs—identically to Eq. (2). The models trained under the semi-exact scheme, denoted GNN*, represent a best case scenario of the models trained using Eq. (3), and will therefore allow us to assess the impact of the dataset quality on the accuracy of the predictions.

We propose the GNN architecture detailed in Supplementary Material. In a nutshell, the GNN is a nonlinear function $f(x_i(t), x_{\mathcal{N}_i}(t))$ that receives the state of a node i and the

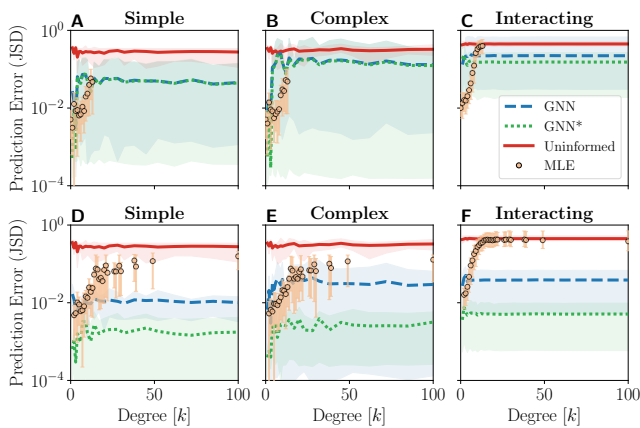


FIG. 2. (color online) **Evaluation of the extrapolation capability of GNNs trained on Erdős-Rényi (ER, top row) and Barabási-Albert (BA, bottom row) random networks [38] for the (A, D) simple, (B, E) complex and (C, F) interacting contagion dynamics.** The dashed lines correspond to the GNN prediction error, i.e. the average Jensen-Shannon distance (JSD) between the LTPs of the dynamics used to generate the training datasets (labeled as GT for “ground truth”) and the predictions of the GNNs trained with these datasets. Similarly, the dotted lines correspond to the JSD error of GNN trained on the same datasets but using a semi-exact training scheme (denoted by GNN*). For comparison, the solid lines correspond to the JSD error of an uninformed baseline in which all local transitions are equiprobable, i.e. $p_{\sigma}^{\mu \rightarrow \nu} = |\Omega|^{-1}$ where $|\Omega|$ is the number of node states. The prediction error of the MLEs is shown with markers to clearly illustrate where data is lacking in the training datasets. Lines and markers were obtained by averaging the JSD errors over every σ corresponding to a same value of k . The standard deviation around these average values is shown with a colored area around the lines and with vertical bars for the markers. The training datasets are generated using a ER or BA network composed of $|\mathcal{V}| = 1000$ nodes and with average degree $\langle k \rangle = 4$. We used the same parameters as on Fig. 1 for the simple and complex contagion dynamics, and used $(\tau_1, \tau_2, \gamma_1, \gamma_2, \zeta) = (0.02, 0.01, 0.12, 0.13, 10)$ for the interacting contagion dynamics. All technical details related to training are provided in Supplementary Material.

states of its neighbors \mathcal{N}_i , and then returns the LTPs providing the probabilities for nodes i to be in each of the available states at $t + \Delta t$,

$$f(x_i(t), x_{\mathcal{N}_i}(t)) = \left(\hat{p}_{x_{\mathcal{N}_i}(t)}^{x_i(t) \rightarrow \nu} \right)_{\nu \in \Omega}. \quad (4)$$

This function is identical for all nodes and, in practice, the GNN is applied in parallel to every node. To allow the GNN to be applicable to any neighborhood size, the states of the neighbors are aggregated with an attention mechanism inspired by [40]. A notable advantage of this GNN architecture is its *inductive nature*: It learns how to combine the states of the neighbors locally, i.e. through the edges of the network. It is therefore independent from the global network structure, and can consequently be used on any network structure once it has been trained.

We illustrate our approach by applying it to three types of stochastic contagion dynamics whose behaviors heavily

depend on the structure of the underlying network [3, 12, 41]. We first consider a *simple contagion* dynamics: The discrete-time susceptible-infected-susceptible (SIS) dynamics in which nodes are either susceptible (S) or infected (I). At each time step, infected nodes transmit the disease to each of their susceptible neighbors with probability τ , and recover from the disease with probability γ , thus becoming susceptible again. The LTPs of this dynamics are

$$p_{\ell}^{S \rightarrow I} = 1 - p_{\ell}^{S \rightarrow S} = 1 - (1 - \tau)^{\ell} \quad (5a)$$

$$p_{\ell}^{I \rightarrow S} = 1 - p_{\ell}^{I \rightarrow I} = \gamma. \quad (5b)$$

Note that the state of the neighbors of a node, σ , is fully specified by the number of infected neighbors, ℓ . We stress that the GNN is not a priori designed to compute the LTPs as a function of ℓ , but rather computes them as a function of the complete state of the neighbors, σ . The GNN must therefore *learn* that the number of infected neighbor is sufficient to compute the LTPs.

Equation (5a) assumes that disease transmission events are independent. In other words, the probability for a susceptible node to be infected by any of its infectious neighbors does not depend on the state of its other neighbors. The second dynamical process we consider lifts this assumption by replacing Eq. (5a) with the “Planck-like” nonmonotonic infection probability

$$p_{\ell}^{S \rightarrow I} = \frac{1}{z(\eta)} \frac{\ell^3}{e^{\ell/\eta} - 1}, \quad (6)$$

where $z(\eta)$ is fixed such that $p_{\ell}^{S \rightarrow I}$ equals 1 at its maximum, the position of this maximum being controlled by the parameter $\eta > 0$. We refer to this second dynamics as *complex* [43] since transmission is now a nonlinear process that depends on the state of the other neighbors of a node. While unrealistic in the context of disease spreading, Eq. (6) has an interesting interpretation in the context of the propagation of a social behavior. The probability that an individual adopts a new behavior increases monotonously with its number of friends that have adopted the behavior if it appears new or scarce (low ℓ). However, the same individual will become reluctant to adopt this behavior if it has become mainstream and popular (high ℓ), resulting in monotonously decreasing probability of adoption.

The third contagion dynamics we consider is an extension of the SIS dynamics to two interacting infectious diseases in which nodes can be in four different states: Susceptible to both diseases ($S_1 S_2$), infected by one disease and susceptible to the other ($I_1 S_2$ or $S_1 I_2$), or infected by both diseases ($I_1 I_2$). Like the SIS dynamics, nodes infected by disease g will transmit it to a susceptible neighbor with probability τ_g and will recover from g with probability γ_g . The interaction between the two diseases affects the probability of transmission whenever either node, the infected or the susceptible one, is already infected by the other disease. A node infected by disease g will then infect its neighbor susceptible to g with probability $\zeta \tau_g$, where ζ controls the strength of the interaction between the two diseases. This *interacting contagion dynamics* is encoded in 12 LTPs similar to Eqs. (5) whose expressions are given in Supplementary Material.

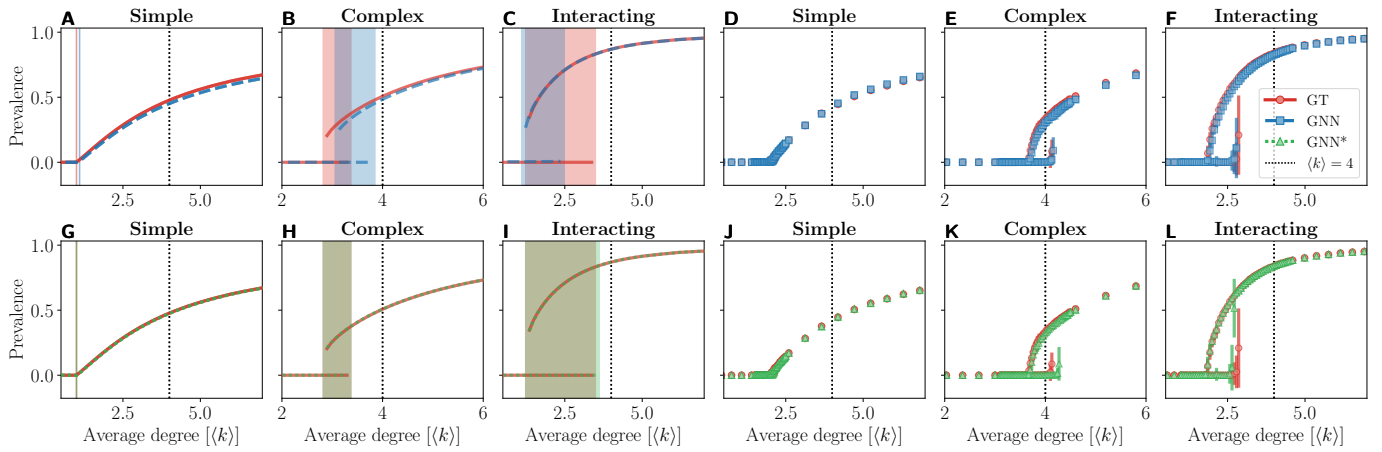


FIG. 3. **Bifurcation diagrams of the simple, complex and interacting contagion dynamics on Poisson networks [38] composed of $|\mathcal{V}| = 2000$ nodes with different average degrees $\langle k \rangle$.** Prevalence is defined as the fraction of nodes infected by at least one disease. Panels (A–C) and (G–I) show the steady-state prevalence obtained by solving a set of mean-field equations adapted from Ref. [42] (see Supplementary Material). The solid vertical lines indicate the critical points where a steady state changes its stability; a colored area is used to indicate the bistable regime that exists when the two steady states do not change their stability simultaneously. Panels (D–F) and (J–L) show the steady-state prevalence obtained by standard stochastic numerical simulations; each marker is averaged over 100 simulations and the vertical bars show the standard deviation. Red lines, markers and areas are obtained by using the LTPs of the original dynamics (labeled as GT for “ground truth”) in the mean-field equations as well as in the numerical simulations. Blue lines, markers and areas (first row) are obtained by using the LTPs inferred with the GNN trained on a dataset generated with a Barabási-Albert network composed of $|\mathcal{V}| = 1000$ nodes and with average degree $\langle k \rangle = 4$ (value indicated by a vertical dotted black line for reference). Green lines, markers and areas (second row) are obtained by using the LTPs inferred with the GNN trained on the same dataset but using a semi-exact training scheme (denoted by GNN*). The parameters of the contagion dynamics are the same as for Figs. 1 and 2.

In Fig. 1, we show the LTPs predicted by the GNN and compare them with Eqs. (5)–(6) as well as with the maximum likelihood estimators (MLEs) of $p_{\sigma}^{\mu \rightarrow \nu}$. The MLEs are computed from the time series and correspond to the frequency at which nodes in state μ with neighborhood σ transition to ν at the next time step. We find that the GNN fits remarkably well the LTPs of the simple and complex contagion dynamics. In fact, we found the predictions of the GNN to be systematically smoother than the ones provided by the MLEs. This is because the MLEs estimate the LTPs for each individual pair (μ, σ) from disjoint subsets of the training dataset. This implies that a large number of samples of each pair (μ, σ) is needed for the MLEs to provide accurate estimates of every LTPs; a condition rarely met in realistic settings, especially for high degree nodes. This also means that the MLE cannot interpolate in between nor can it extrapolate beyond the pairs (μ, σ) present in the training dataset. In contrast, the GNN works in a conceptually different manner: It is differentiable by construction and all parameters are hierarchically involved in the estimation of the LTPs. Its predictions are therefore smoother, more consistent and able to inter- or extrapolate beyond the training dataset. It also means that the GNN benefits from any sample to improve its predictions for all LTPs.

Figure 2 addresses the accuracy of the predictions of the GNN for *unseen* local network structures, i.e. predictions of LTPs corresponding to pairs (μ, σ) that are not necessarily present from the training dataset. These predictions were extracted from the GNN by applying it to a star graph of $k + 1$ nodes— k nodes of degree 1 connected to a central node of

degree k . Because σ is typically multivariate, and thus cannot be summarized by a single scalar ℓ as for the simple and complex contagion dynamics presented in Fig. 1—it is three-dimensional for the interacting contagion dynamics—, we use the Jensen-Shannon distance (JSD) [37] to quantify the similarity between the LTPs predicted by the GNN and the “ground truth”. Figure 2 shows averages of the JSD, with standard deviations, over all possible neighborhoods σ and states μ for various values of k . Note that the JSD is similar to the loss function of Eq. (2), but it has the notable advantages of being symmetrical, of being more forgiving if a LTP is wrongly predicted to be equal to zero (something that happens with MLEs), and of allowing meaningful comparisons between more than two distributions at the same time (by virtue of being a metric).

Figure 2 confirms that the GNN provides more accurate predictions than MLEs in general. This is especially true in the case of the interacting contagion on BA networks, where MLEs are only marginally different from the uninformed baseline for high degree nodes. This is a consequence of how scarce the inputs are for this dynamics compared to both the simple and complex contagion dynamics for training datasets of the same size, and of how fast the size of the set of possible inputs scales, thereby quickly rendering MLEs completely ineffective for small training datasets. Figure 2(F) therefore provides a telling illustration of the challenge of inferring the parameters of slightly complex contagion models from limited data. The GNN, on the other hand, is less affected by the scarcity of the data, since any sample improves

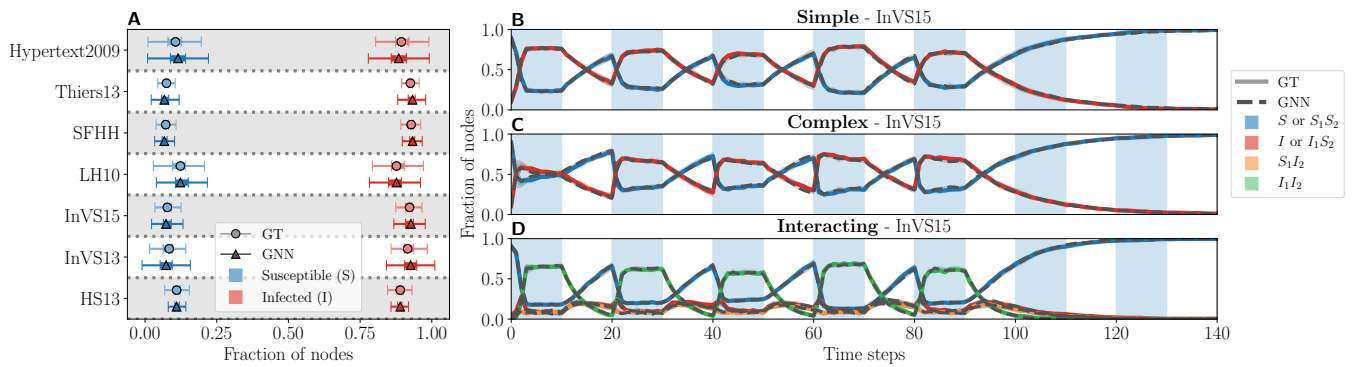


FIG. 4. (color online) **Projection on real-world temporal networks of proximity contacts between individuals in conferences (Hypertext 2009, SFHH), workplaces (InVS13, InVS15), schools (Thiers13, HS13) and hospitals (LH10) [44–46].** (A) Steady-state fraction of susceptible nodes (in blue) and of infected nodes (in red) for the simple contagion dynamics on the aggregated version of these temporal networks. Triangles correspond numerical simulations averaged over 100 realizations obtained using the same LTPs as in Fig. 3(A, D). Circles show the results of numerical simulations performed with the “ground truth” LTPs of the original dynamics. (B–D) Numerical simulations of the (B) simple, (C) complex and (D) interacting contagion dynamics over time on the workplace InVS15 temporal network, averaged over 100 realizations. Solid lines used the “ground truth” LTPs, and dashed lines used the LTPs extracted from the GNN (the same LTPs as in Fig. 3). Colored areas around the lines indicate the standard deviation. Alternating white and blue zones indicates the time windows, each of which consisting of 10 time steps of the original dataset. Results for the other temporal networks are available in Supplementary Material.

the predictions for all LTPs, as discussed above. In fact, the GNN accuracy is often close to the best case scenario, illustrated by the GNN*, trained under similar conditions but with a semi-exact training scheme.

Figure 2 also suggests that the underlying network structure of the training dataset (mainly its degree distribution) plays a crucial role in the accuracy of the GNN’s predictions for unseen local structures. Indeed, our results show that the GNN provides more accurate predictions when interpolating in between observed values of k than when extrapolating for values of k higher than those present in the training dataset. In other words, it is *easier* for the GNN to interpolate in-between “landmarks” provided by the dataset than to extrapolate beyond the training dataset without any bearings whatsoever. Heterogeneous networks, like Barabási-Albert networks, are therefore expected to yield accurate predictions over a wider range of local structures (μ , σ) than homogeneous networks, even if the training datasets are similar in size. This is also supported by the fact that the best case scenario in terms of GNN accuracy (GNN*) is significantly poorer for homogeneous networks [Figs. 2(A–C)] than for heterogeneous networks [Figs. 2(D–F)]. The amount of *valuable information* contained in a given dataset could therefore be interpreted through the lens of the properties of the training dataset’s underlying network structure. Altogether, these findings suggest a wide applicability of our approach for real complex systems, whose underlying network structures recurrently exhibit a heterogeneous degree distribution [47].

To further illustrate the inductive nature of our GNN architecture, we use it to recover the bifurcation diagram of the three contagion dynamics and to project their behaviors on real-world networks. In the infinite-size limit $|\mathcal{V}| \rightarrow \infty$, these dynamics have two possible steady states: the absorbing state where all nodes are susceptible, and the endemic state in which a fraction of nodes remains infected over

time [3, 12, 41]. These steady states exchange stability during a phase transition which is continuous for the simple contagion and discontinuous for the complex and interacting contagion dynamics. The position of the phase transition depends both on the parameters of the dynamics and on the topology of the network on which they take place. Note that for the complex and interacting contagion dynamics, the stability of absorbing and endemic states do not change at the same point, giving rise to a bistable regime where both states are stable.

Figure 3 shows the bifurcation diagrams obtained by analyzing a mean field framework which uses the LTPs extracted from the GNN, as well as those obtained by performing numerical simulations with these same LTPs. In particular, the mean field perspective demonstrates the possibility to develop an approximate representation of the GNN predictions that, although not as accurate as the predictions obtained by numerical simulations, is amenable to mathematical analysis (i.e. position of fixed points, their stability and the critical thresholds of the phase transitions). The first row of Fig. 3 shows that the GNN correctly predicts whether the phase transition is continuous or discontinuous, as well as the existence of a bistable regime. Quantitatively, the predictions are also strikingly accurate—essentially perfectly accurate for the simple contagion dynamics—which is remarkable given that the bifurcation diagrams were obtained on networks the GNN had never seen before. The second row of Fig. 3 shows the same bifurcation diagrams but using GNN* models trained under the semi-exact training scheme. The almost perfect overlap and thresholds of the curves indicates that there is virtually no intrinsic limit to the accuracy the GNN’s predictions, and highlights once more the critical influence of the information contained in the training dataset. In other words, our GNN’s architecture is as accurate as its training data allows it to be.

Finally, similar levels of accuracy are obtained when simulating the three contagion dynamics on static [Fig. 4(A)] and

temporal [Figs. 4(B–D)] real-world complex networks. Recall that the GNN used to produce these results is the same as the one used in Fig. 3, and was trained on a synthetic static network of a different size. The projections obtained from the GNN remain in the same vicinity as those generated by the “ground truth” LTPs throughout the timespan of the dataset, and show similar patterns of population infections/recoveries when the configuration of the network changes.

In summary, we introduced a data-driven approach that learns the effective mechanisms governing the propagation of contagion dynamics on complex networks. We proposed a reliable training protocol, and we validated the projections of our GNN architecture on simple, complex and interacting contagion dynamics using synthetic as well as real-world static and temporal complex networks. Interestingly, we found that our approach performs better when trained on data whose underlying network structure is heterogeneous, which could prove useful in real-world applications of our method given the ubiquitousness of scale-free networks [47].

By recovering the bifurcation diagram of various dynamics, we illustrated how our approach can leverage time series from an unknown dynamical process to gain insights about

its properties—the existence of a phase transition and its order. Most importantly, we showed how to explicitly extract the LTPs inferred by the GNN architecture, which in turn can help uncover the underlying mechanisms governing the dynamics and help build effective mechanistic models. In a way, we see this approach as the equivalent of a numerical Petri dish—offering a new way to experiment and gain insights about an unknown contagion dynamics—that is complementary to traditional mechanistic modeling.

Although we focused the presentation of our method on contagion dynamics, its potential applicability reaches many other realms of complex systems modeling where intricate mechanisms are at play. We believe this work establishes solid foundations for the use of deep learning in the design of more effective realistic models of complex systems.

We are grateful to Emily Cyr and Guillaume St-Onge for helpful comments and to François Thibault, Patrick Desrosiers, Louis J. Dubé, Simon Hardy and Laurent Hébert-Dufresne for fruitful discussions. This work was supported by the Sentinelle Nord initiative from the Canada First Research Excellence Fund (CM, EL, AA), the Conseil de recherches en sciences naturelles et en génie du Canada (CM, AA) and the Fonds de recherche du Québec-Nature et technologie (EL).

-
- [1] W. O. Kermack and A. G. McKendrick, “A Contribution to the Mathematical Theory of Epidemics,” *Proc. R. Soc. A* **115**, 700–721 (1927).
- [2] H. W. Hethcote, “The Mathematics of Infectious Diseases,” *SIAM Rev.* **42**, 599–653 (2000).
- [3] I. Z. Kiss, J. C. Miller, and P. L. Simon, *Mathematics of Epidemics on Networks* (Springer, 2017) p. 598.
- [4] F. Brauer, C. Castillo-Chavez, and Z. Feng, *Mathematical Models in Epidemiology* (Springer, 2019).
- [5] C. I. Siettos and L. Russo, “Mathematical modeling of infectious disease dynamics,” *Virulence* **4**, 295–306 (2013).
- [6] N. C. Grassly and C. Fraser, “Mathematical models of infectious disease transmission,” *Nat. Rev. Microbiol.* **6**, 477–487 (2008).
- [7] A. Pastore y Piontti, N. Perra, L. Rossi, N. Samay, and A. Vespignani, *Charting the Next Pandemic: Modeling Infectious Disease Spreading in the Data Science Age* (Springer, 2019).
- [8] C. Viboud and A. Vespignani, “The future of influenza forecasts,” *Proc. Natl. Acad. Sci. U.S.A.* **116**, 2802–2804 (2019).
- [9] L. Hébert-Dufresne, S. V. Scarpino, and J.-G. Young, “Macroscopic patterns of interacting contagions are indistinguishable from social reinforcement,” *Nat. Phys.* **16**, 426–431 (2020).
- [10] S. Nickbakhsh, C. Mair, L. Matthews, R. Reeve, P. C. D. Johnson, F. Thorburn, B. von Wissmann, A. Reynolds, J. McMenamin, R. N. Gunson, and P. R. Murcia, “Virus–virus interactions impact the population dynamics of influenza and the common cold,” *Proc. Natl. Acad. Sci. U.S.A.* **116**, 27142–27150 (2019).
- [11] D. M. Morens, J. K. Taubenberger, and A. S. Fauci, “Predominant Role of Bacterial Pneumonia as a Cause of Death in Pandemic Influenza: Implications for Pandemic Influenza Preparedness,” *J. Infect. Dis.* **198**, 962–970 (2008).
- [12] J. Sanz, C.-Y. Xia, S. Meloni, and Y. Moreno, “Dynamics of Interacting Diseases,” *Phys. Rev. X* **4**, 041005 (2014).
- [13] D. Centola, “The Spread of Behavior in an Online Social Network Experiment,” *Science* **329**, 1194–1197 (2010).
- [14] S. Lehmann and Y.-Y. Ahn, eds., *Complex Spreading Phenomena in Social Systems*, Computational Social Sciences (Springer, 2018).
- [15] I. Iacopini, G. Petri, A. Barrat, and V. Latora, “Simplicial models of social contagion,” *Nat. Commun.* **10**, 2485 (2019).
- [16] I. Goodfellow, Y. Bengio, and A. Courville, *Deep Learning* (MIT Press, 2016).
- [17] A. Krizhevsky, I. Sutskever, and G. E. Hinton, “ImageNet Classification with Deep Convolutional Neural Networks,” in *NIPS Proc.* (2012) pp. 1097–1105.
- [18] A. Vaswani, N. Shazeer, N. Parmar, J. Uszkoreit, L. Jones, A. N. Gomez, Ł. Kaiser, and I. Polosukhin, “Attention Is All You Need,” in *Adv. Neural Inf. Process. Syst. 30 (NIPS 2017)* (2017) pp. 5998–6008.
- [19] M. Långkvist, L. Karlsson, and A. Loutfi, “A review of unsupervised feature learning and deep learning for time-series modeling,” *Pattern Recognit. Lett.* **42**, 11–24 (2014).
- [20] Z. Zhang, P. Cui, and W. Zhu, “Deep Learning on Graphs: A Survey,” (2018), [arXiv:1812.04202](https://arxiv.org/abs/1812.04202).
- [21] J. Zhou, Gé Cui, Z. Zhang, C. Yang, Z. Liu, L. Wang, C. Li, and M. Sun, “Graph Neural Networks: A Review of Methods and Applications,” (2018), [arXiv:1812.08434](https://arxiv.org/abs/1812.08434).
- [22] K. Xu, W. Hu, J. Leskovec, and S. Jegelka, “How Powerful are Graph Neural Networks?” (2019), [arXiv:1810.00826](https://arxiv.org/abs/1810.00826).
- [23] W. L. Hamilton, R. Ying, and J. Leskovec, “Representation Learning on Graphs: Methods and Applications,” (2017), [arXiv:1709.05584](https://arxiv.org/abs/1709.05584).
- [24] M. Balakrishnan and G. T. V, “A neural network framework for predicting dynamic variations in heterogeneous social networks,” *PLOS ONE* **15**, e0231842 (2020).
- [25] F. A. Rodrigues, T. Peron, C. Connaughton, J. Kurths,

- and Y. Moreno, “A machine learning approach to predicting dynamical observables from network structure,” (2019), [arXiv:1910.00544](#).
- [26] Z. Zhang, Y. Zhao, J. Liu, S. Wang, R. Tao, R. Xin, and J. Zhang, “A general deep learning framework for network reconstruction and dynamics learning,” *Appl. Netw. Sci.* **4**, 110 (2019).
- [27] E. Laurence, C. Murphy, G. St-Onge, X. Roy-Pomerleau, and V. Thibeault, “Detecting structural perturbations from time series with deep learning,” (2020), [arXiv:2006.05232](#).
- [28] A. Fout, J. Byrd, B. Shariat, and A. Ben-Hur, “Protein Interface Prediction using Graph Convolutional Networks,” in *Adv. Neural Inf. Process. Syst.* **30** (2017) pp. 6530–6539.
- [29] M. Zitnik, M. Agrawal, and J. Leskovec, “Modeling polypharmacy side effects with graph convolutional networks,” in *Bioinformatics*, Vol. 34 (2018) pp. i457–i466.
- [30] F. Altarelli, A. Braunstein, L. Dall’Asta, A. Lage-Castellanos, R. Zecchina, L. Dall’Asta, A. Lage-Castellanos, and R. Zecchina, “Bayesian Inference of Epidemics on Networks via Belief Propagation,” *Phys. Rev. Lett.* **112**, 118701 (2014).
- [31] R. Dutta, A. Mira, and J.-P. Onnela, “Bayesian inference of spreading processes on networks,” *Proc. R. Soc. A* **474**, 20180129 (2018).
- [32] P. Eichelsbacher and A. Ganesh, “Bayesian Inference for Markov Chains,” *J. Appl. Probab.* **39**, 91–99 (2002).
- [33] G. Cybenko, “Approximation by superpositions of a sigmoidal function,” *Math. Control. Signals, Syst.* **2**, 303–314 (1989).
- [34] K. Hornik, “Approximation capabilities of multilayer feedforward networks,” *Neural Networks* **4**, 251–257 (1991).
- [35] D. E. Rumelhart, G. E. Hinton, and R. J. Williams, “Learning representations by back-propagating errors,” *Nature* **323**, 533–536 (1986).
- [36] D. P. Kingma and J. Ba, “Adam: A Method for Stochastic Optimization,” (2014), [arXiv:1412.6980](#).
- [37] T. M. Cover and J. A. Thomas, *Elements of Information Theory*, 2nd ed. (Wiley-Interscience, 2005) p. 776.
- [38] A.-L. Barabási, *Network Science* (Cambridge University Press, 2016) p. 474.
- [39] R. Y. Rubinstein and D. P. Kroese, *Simul. Monte Carlo Method*, 3rd ed. (Wiley, 2016) pp. 1–414.
- [40] P. Velickovi, G. Cucurull, A. Casanova, A. Romero, P. Li, and Y. Bengio, “Graph attention networks,” in *International Conference on Learning Representations* (2018).
- [41] R. Pastor-Satorras, C. Castellano, P. Van Mieghem, and A. Vespignani, “Epidemic processes in complex networks,” *Rev. Mod. Phys.* **87**, 925–979 (2015).
- [42] P. G. Fennell and J. P. Gleeson, “Multistate Dynamical Processes on Networks: Analysis through Degree-Based Approximation Frameworks,” *SIAM Rev.* **61**, 92–118 (2019).
- [43] S. Lehmann and Y.-Y. Ahn, eds., *Complex Spreading Phenomena in Social Systems* (Springer, 2018) p. 368.
- [44] L. Isella, J. Stehlé, A. Barrat, C. Cattuto, J.-F. Pinton, and W. Van den Broeck, “What’s in a crowd? Analysis of face-to-face behavioral networks,” *J. Theor. Biol.* **271**, 166–180 (2011).
- [45] R. Mastrandrea, J. Fournet, and A. Barrat, “Contact Patterns in a High School: A Comparison between Data Collected Using Wearable Sensors, Contact Diaries and Friendship Surveys,” *PLOS ONE* **10**, e0136497 (2015).
- [46] M. Génois and A. Barrat, “Can co-location be used as a proxy for face-to-face contacts?” *EPJ Data Sci.* **7**, 11 (2018).
- [47] I. Voitalov, P. van der Hoorn, R. van der Hofstad, and D. Krioukov, “Scale-free networks well done,” *Phys. Rev. Research* **1**, 033034 (2019).

Deep learning of stochastic contagion dynamics on complex networks

— Supplementary Material —

Charles Murphy, Edward Laurence, and Antoine Allard

Département de Physique, de Génie Physique, et d'Optique,

Université Laval, Québec (Québec), Canada G1V 0A6 and

Centre interdisciplinaire en modélisation mathématique,

Université Laval, Québec (Québec), Canada G1V 0A6

(Dated: June 13, 2020)

CONTENTS

I. Model	2
A. Details of the Architecture	2
B. Attention Mechanism	2
II. Projections on Real-World Temporal Networks	5
III. Local Transition Probabilities of the Interacting Contagion Dynamics	6
IV. Loss Optimization Patterns	8
V. Dataset Generation	9
A. Algorithm	9
B. Impact of the Data Generation Hyperparameters	11
VI. Training Settings	14
A. Optimization	14
B. Validation Dataset Selection	14
C. Hyperparameters	15
VII. Mean Field framework	15
A. Approximate master equations	15
B. Numerical Evaluation of the Thresholds	16
References	17

I. MODEL

A. Details of the Architecture

We propose the graph neural network (GNN) architecture shown in Fig. 1. First, we apply a sequence of input layers to the state of each node, denoted $x_i(t)$, individually to transform them into features. A single layer l with f_l features is composed of a linear transformation and a rectified linear unit activation function (ReLU, expressed as $\text{ReLU}(x) = \max\{x, 0\}$) and acts on a feature vector \mathbf{u}_i^{l-1} such that

$$\mathbf{u}_i^l = \text{ReLU}\left(\mathbf{W}^l \mathbf{u}_i^{l-1} + \mathbf{b}^l\right) \quad (1)$$

where $\mathbf{W}^l \in \mathbb{R}^{f_l \times f_{l-1}}$ and $\mathbf{b}^l \in \mathbb{R}^{f_l}$ are trainable parameters. After these first layers, the resulting feature vectors are aggregated using a graph attention module inspired by Ref. [1] (Description in Sec. IB). In short, the graph attention module, illustrated in blue in Fig. 1, is a trainable nonlinear function, denoted \mathcal{A} , which combines the node feature vectors using the adjacency matrix \mathbf{A} . This layer returns a set of new feature vectors describing *both* the state of nodes and the states of their first neighbors. The aggregated features are then processed into a set of final feature vectors, namely $\mathbf{v}_i \in \mathbb{R}^{|\Omega|}$, with another sequence of output layers composed of linear transformations and a ReLU activation functions [similar to Eq. (1)]. From the aggregated and transformed feature vectors \mathbf{v}_i , we finally compute a discrete probability distribution, using a Softmax function, corresponding to the local transition probabilities (LTPs) of the GNN, where each probability is expressed as following:

$$\hat{p}_{i;\nu} = [\text{Softmax}(\mathbf{v}_i)]_\nu = \frac{\exp([\mathbf{v}_i]_\nu)}{\sum_{\xi=1}^{|\Omega|} \exp([\mathbf{v}_i]_\xi)}. \quad (2)$$

Recall that each entry $\hat{p}_{i;\nu}$ of this probability distribution corresponds to the probability that node i transition to state ν , which is conditioned on its state $x_i(t)$ and the state of its first neighbors $x_{\mathcal{N}_i}(t)$ thanks to the GNN architecture. Using the notation that we used in the main paper, we get the following equivalence:

$$\hat{p}_{i;\nu} = \hat{p}_{i;\nu}(t) \equiv \hat{p}_{x_{\mathcal{N}_i}(t)}^{x_i(t) \rightarrow \nu}. \quad (3)$$

We summarize the architecture of the GNN models for each contagion dynamics we used in the main paper in Tab. I.

B. Attention Mechanism

Our attention mechanism is a variant of the recently introduced graph attention networks (GAT) [1] and corresponds to a nonlinear trainable function \mathcal{A} that combines the feature vectors of the nodes with respect

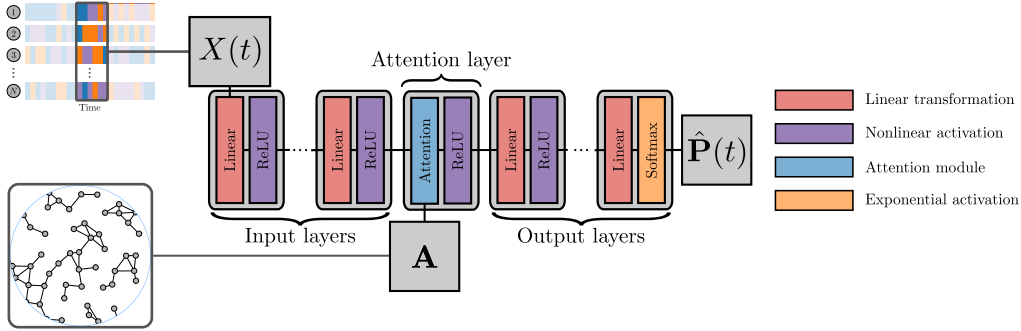


FIG. 1. (color online) **Illustration of the GNN architecture.** The blocks of different colors represent a GNN operations. The red blocks correspond to trainable linear transformation parametrized by weights and biases (see text). The purple blocks represent non-trainable activation function between each layer. The core of the model is the attention module [1], which is represented in blue. The orange block at the end is an exponential Softmax activation that transforms the output into properly normalized transition probabilities.

Dynamics	Simple contagion	Complex contagion	Interacting contagion
Input layers			Linear(1, 32)
	Linear(1, 32)	Linear(1, 32)	ReLU
	ReLU	ReLU	Linear(32, 32)
	Linear(32, 32)	Linear(32, 32)	ReLU
	ReLU	ReLU	Linear(32, 32)
Number of attention layers	1	1	2
Output layers			Linear(32, 32)
	Linear(32, 32)	Linear(32, 32)	ReLU
	ReLU	ReLU	Linear(32, 32)
	Linear(32, 2)	Linear(32, 2)	ReLU
	Softmax	Softmax	Linear(32, 4)
Number of parameters	2307	2307	6630

TABLE I. **Layer by layer description of the GNN models for each contagion dynamics.** For each sequence, the operations are applied from top to bottom. The operations represented by Linear(m, n) correspond to linear transformations of the form $f(\mathbf{x}) = \mathbf{W}\mathbf{x} + \mathbf{b}$, where $\mathbf{x} \in \mathbb{R}^m$ is the input, $\mathbf{W} \in \mathbb{R}^{n \times m}$ and $\mathbf{b} \in \mathbb{R}^n$ are trainable parameters. The operations ReLU and Softmax are activation functions given by $\text{ReLU}(x) = \max\{x, 0\}$ and $\text{Softmax}(\mathbf{x}) = \frac{\exp(\mathbf{x})}{\sum_i \exp(x_i)}$.

to the adjacency matrix \mathbf{A} . It works by assigning an attention coefficient α_{ij} that modulates the effect of the node j features over the node i resulting features. Considering the pair of connected nodes (i, j) whose input feature vectors are respectively \mathbf{u}_i^l and \mathbf{u}_j^l , we compute the attention coefficient α_{ij} using the following expression:

$$\alpha_{ij} = \sigma \left[\mathbf{W}^{\mathcal{A}} \left(\mathbf{u}_i^l \parallel \mathbf{u}_j^l \right) + \mathbf{b}^{\mathcal{A}} \right] \quad (4)$$

where

$$\sigma(x) = \frac{1}{1 + e^{-x}} \quad (5)$$

is the logistic function, $\mathbf{W}^{\mathcal{A}} \in \mathbb{R}^{1 \times 2f_l}$ and $\mathbf{b}^{\mathcal{A}} \in \mathbb{R}$ are additional trainable parameters corresponding to a linear transformation and \parallel denotes a concatenation. The logistic function acts as an activation function guaranteeing that the attention coefficients range between 0 (no attention) and 1 (full attention). The attention coefficients are then used to compute the aggregated features \mathbf{v}_i as follows:

$$\mathbf{v}_i = \left[\mathcal{A} \left(\mathbf{u}_1, \dots, \mathbf{u}_N; \mathbf{A} \right) \right]_i = \mathbf{u}_i + \sum_{j \in \mathcal{N}_i} \alpha_{ij} \mathbf{u}_j. \quad (6)$$

Note that our attention mechanism is different from the original GAT from Ref. [1] in two ways. First, in the original paper, they used a Softmax function in Eq. (4) instead of a logistic function, which constrains the attention coefficients to be normalized, i.e. $\sum_j \alpha_{ij} = 1$. Under this constraint, Eq. (6) becomes an averaging operation rather than a general weighted sum. We argue that this normalization constraint is detrimental in the case of learning contagion dynamics specifically, because it does not capture the individual contribution of each neighbors in an absolute way. Rather, it captures the relative contributions of the neighbors with respect to each other—the features of an "average" neighbor—which is more desirable in network embedding tasks [2]. This difference also allows us to enforce a complete self-attention ($\alpha_{ii} = 1$), as one can deduce from Eq. (6). Second, contrary to the original GAT architecture, we do not apply an activation function directly after the linear transformation in Eq. (4). The reason for this is that negative-valued features are, for us, of great importance, because they lead to small attention coefficients. Applying a nonlinear activation function, e.g. a ReLU function, inhibits the negative values and, consequently, prevents the attention coefficients to vanish when needed.

In Ref. [1], they also showed how using multiple attention layers in parallel and in series can be beneficial to network embedding tasks. We also consider using attention layers in parallel in our GNN architecture. To do so, we apply multiple attention layers, denoted \mathcal{A}^q with $q = 1..Q$, on each input feature vectors \mathbf{u}_i , and concatenate the resulting outputs in a single feature vector \mathbf{v}_i as follows:

$$\mathbf{v}_i = \left\| \left\|_{q=1}^Q \left[\mathcal{A}^q \left(\mathbf{u}_1, \dots, \mathbf{u}_N; \mathbf{A} \right) \right] \right\|_i \quad (7)$$

Name	Number of nodes	Number of edges	Timespan [s]	Reference
Hypertext 2009	113	2196	212341	[3]
Thiers13	328	43496	380421	[4]
SFHH	403	73557	106541	[4]
LH10	72	1381	259181	[4]
InVS13	95	3915	993561	[4]
InVS15	219	16725	993561	[4]
HS13	327	5818	363561	[5]

TABLE II. **Properties of social contact networks.** We show the number of nodes, the total number of edges observed and the timespan (in seconds) of these time-varying networks. In Refs. [3–5], they collected these networks by monitoring the proximity of pairs of individuals: If two individuals are in close proximity for at least 20 seconds, a contact (or an edge) is recorded at this time.

During experiments, we also considered applying attention layers in series, but it turns out that in our case using more than one attention layer leads to overfitting. Indeed, recall that the first attention layer aggregates the node features with respect to their first neighbors. Therefore, applying a second attention layer indirectly aggregate the features of the second neighbors, which in turn assumes that their contribution matters in the computation of the LTPs. Because only the first neighbors actually contribute to the true LTPs, it forces the GNN model to unwind this assumption during its training, which is actually difficult to do and might explain the overfitting.

II. PROJECTIONS ON REAL-WORLD TEMPORAL NETWORKS

We investigate our GNN architecture capabilities when used on real-world time-varying networks, after they are trained on synthetic data. More precisely, we apply our GNN models on 7 different temporal network datasets, namely networks of social contacts in conferences (labeled Hypertext 2009 and SFHH), workplaces (labeled InVS13 and InVS15), schools (labeled Thiers13 and HS13) and hospitals (labeled LH10) [3–5]: A more detailed description of these datasets is shown in Tab. II. These datasets contain timestamped edges in the form (t_{ij}, i, j) , where t_{ij} corresponds to the time at which edge (i, j) , representing an active contact between individuals i and j , was observed.

In the main paper, we consider two coarse-grained representations of these temporal networks. For the first one, we aggregate all edges at any given times into a single and static network. We use this more convenient representation in Fig. 2 to compute the steady-state distribution of node states. For each dynamics, we sample 100 points from the LTPs of the GNN models (same model as Fig. 3 of the main

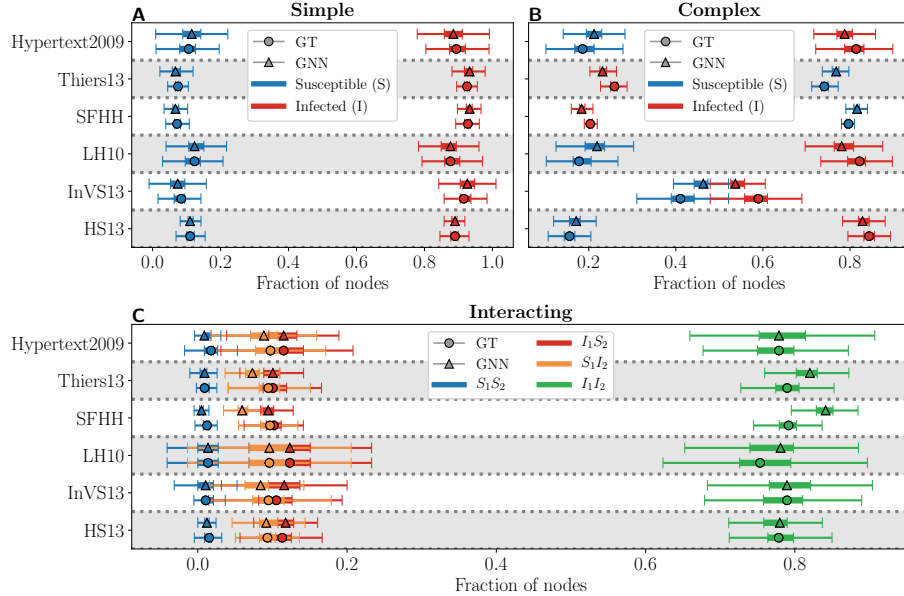


FIG. 2. Steady-state distributions of (a) the simple, (b) the complex and (c) the interacting contagion dynamics on real-world proximity networks in conferences (labeled Hypertext 2009, SFHH), workplaces (labeled InVS13 and InVS15), schools (labeled Thiers13 and HS13) and hospitals (labeled LH10) [3–5]. The steady-state distribution as generated by the LTPs of the GNN models are indicated by the triangles; those generated by the LTPs of the original dynamics (labeled as GT for “ground truth”) are indicated by the circles. The colors of the symbols indicate the state corresponding to the fraction of nodes.

paper) and the LTPs of the original dynamics for comparison, and display the resulting distributions using boxplots.

For the second coarse-grained representation, we aggregate edges in time windows of 12 hours. For instance, a network for which edges are timestamped across 24 hours would result in two different networks—one for the first 12 hours and a second for the remaining 12 hours. We then generate 100 trajectories in which we run the GNN and the ground truth models for 10 time steps per network, i.e. per 12 hours, consequently setting a difference between the network’s and the contagion dynamics’ time scales. It is important to note that we could have chosen arbitrary time scales and window sizes, as setting these time scales differently would change the evolution of the projections. We chose this setting to obtain clear trajectories with potentially small and large variations.

III. LOCAL TRANSITION PROBABILITIES OF THE INTERACTING CONTAGION DYNAMICS

For the interacting contagion dynamics, the support of the state of nodes is $\Omega = \{S_1S_2, I_1S_2, S_1I_2, I_1I_2\}$. The LTPs therefore consist of 16 probabilities—one for each possible transition—, minus the redundant

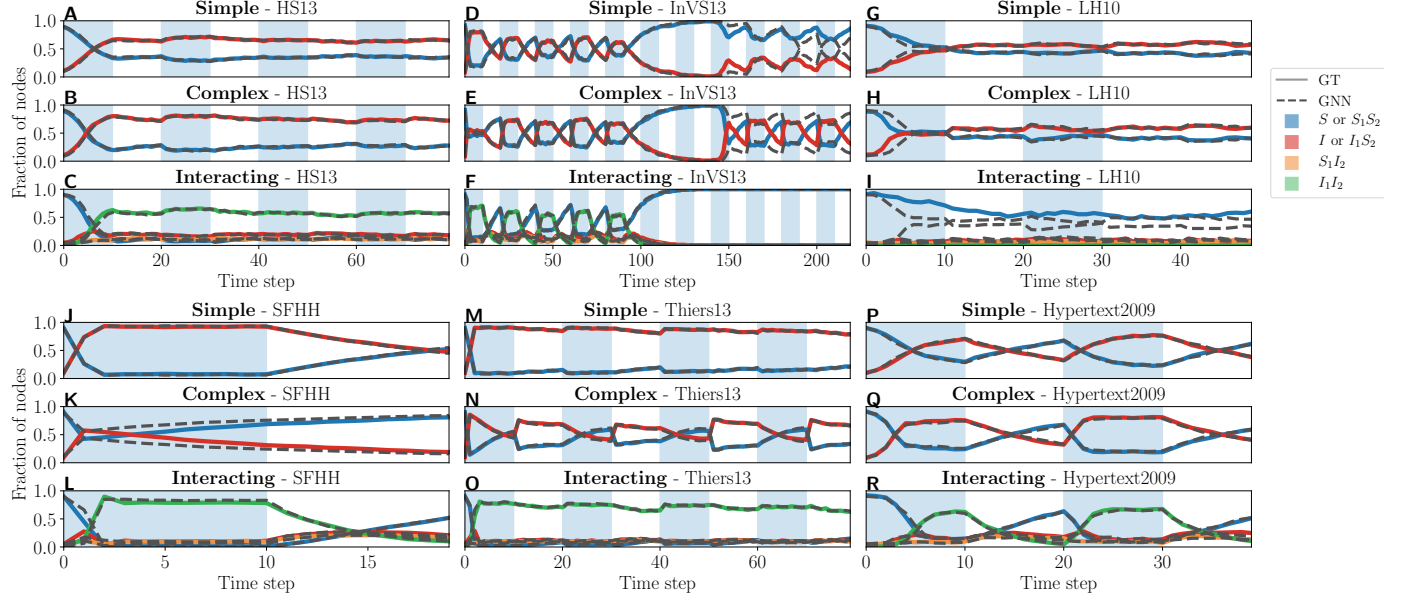


FIG. 3. Projection of (a) the simple, (b) the complex and (c) the interacting contagion dynamics on real-world temporal networks. Panels are organized in triple —one panel per contagion dynamics— corresponding to the same dataset. For instance, panels (a–c) correspond to projections on the HS13 temporal network. Dashed lines correspond to projections when using the LTPs predicted by the GNN model (same as in Fig. 2), while the projections of solid lines used the LTPs of the original dynamics (labeled GT for “ground truth”). Similarly to Fig. 2, colors indicate the state of the fraction of nodes. Changes in shaded area indicate where the network transitioned to its next configuration.

ones obtained from the normalization,

$$\sum_{v \in \Omega} p_{\sigma}^{\mu \rightarrow \nu} = 1, \quad \forall \mu \in \Omega, \forall \sigma \in \Omega^k, \forall k \in \mathbb{Z}^+. \quad (8)$$

Thus there are 12 probabilities in total. Recall that the mechanisms leading to these probabilities are the following: a node infected by disease g transmit the disease to its neighbors susceptible to g with probability τ_g , and recovers from it with probability γ_g , at each time step. If more than one disease is involved in the transmission (from the receiver or the transmitter), the transmission probability is changed to $\zeta \tau_g$, where ζ encodes the coupling the two diseases. From these mechanisms, we obtain the complete distribution of

LTPs. For the transitions from the completely susceptible state, S_1S_2 , the LTPs are

$$p_{\ell}^{S_1S_2 \rightarrow I_1S_2} = \left[1 - (1 - \tau_1)^{\ell^{I_1S_2}} (1 - \zeta\tau_1)^{\ell^{I_1I_2}} \right] (1 - \tau_2)^{\ell^{S_1I_2}} (1 - \zeta\tau_2)^{\ell^{I_1I_2}}, \quad (9a)$$

$$p_{\ell}^{S_1S_2 \rightarrow S_1I_2} = (1 - \tau_1)^{\ell^{I_1S_2}} (1 - \zeta\tau_1)^{\ell^{I_1I_2}} \left[1 - (1 - \tau_2)^{\ell^{S_1I_2}} (1 - \zeta\tau_2)^{\ell^{I_1I_2}} \right], \quad (9b)$$

$$p_{\ell}^{S_1S_2 \rightarrow I_1I_2} = \left[1 - (1 - \tau_1)^{\ell^{I_1S_2}} (1 - \zeta\tau_1)^{\ell^{I_1I_2}} \right] \left[1 - (1 - \tau_2)^{\ell^{S_1I_2}} (1 - \zeta\tau_2)^{\ell^{I_1I_2}} \right], \quad (9c)$$

$$p_{\ell}^{S_1S_2 \rightarrow S_1S_2} = 1 - \left[p_{\ell}^{S_1S_2 \rightarrow I_1S_2} + p_{\ell}^{S_1S_2 \rightarrow S_1I_2} + p_{\ell}^{S_1S_2 \rightarrow I_1I_2} \right]. \quad (9d)$$

For the transitions from the state I_1S_2 , i.e. infected by the disease 1, we have

$$p_{\ell}^{I_1S_2 \rightarrow S_1S_2} = \gamma_1 (1 - \zeta\tau_2)^{\ell^{S_1I_2} + \ell^{I_1I_2}}, \quad (10a)$$

$$p_{\ell}^{I_1S_2 \rightarrow S_1I_2} = \gamma_1 \left[1 - (1 - \zeta\tau_2)^{\ell^{S_1I_2} + \ell^{I_1I_2}} \right], \quad (10b)$$

$$p_{\ell}^{I_1S_2 \rightarrow I_1I_2} = (1 - \gamma_1) \left[1 - (1 - \zeta\tau_2)^{\ell^{S_1I_2} + \ell^{I_1I_2}} \right], \quad (10c)$$

$$p_{\ell}^{I_1S_2 \rightarrow I_1S_2} = 1 - \left[p_{\ell}^{I_1S_2 \rightarrow S_1S_2} + p_{\ell}^{I_1S_2 \rightarrow S_1I_2} + p_{\ell}^{I_1S_2 \rightarrow I_1I_2} \right], \quad (10d)$$

and similarly, for the transitions from the state S_1I_2 , i.e. infected by the disease 2,

$$p_{\ell}^{S_1I_2 \rightarrow S_1S_2} = (1 - \zeta\tau_1)^{\ell^{I_1S_1} + \ell^{I_1I_2}} \gamma_2, \quad (11a)$$

$$p_{\ell}^{S_1I_2 \rightarrow I_1S_2} = \left[1 - (1 - \zeta\tau_1)^{\ell^{I_1S_1} + \ell^{I_1I_2}} \right] \gamma_2, \quad (11b)$$

$$p_{\ell}^{S_1I_2 \rightarrow I_1I_2} = \left[1 - (1 - \zeta\tau_1)^{\ell^{I_1S_1} + \ell^{I_1I_2}} \right] (1 - \gamma_2), \quad (11c)$$

$$p_{\ell}^{S_1I_2 \rightarrow S_1I_2} = 1 - \left[p_{\ell}^{S_1I_2 \rightarrow S_1S_2} + p_{\ell}^{S_1I_2 \rightarrow I_1S_2} + p_{\ell}^{S_1I_2 \rightarrow I_1I_2} \right]. \quad (11d)$$

Finally, the LTPs corresponding to the transitions from the state I_1I_2 , i.e. infected by both diseases are

$$p_{\ell}^{I_1I_2 \rightarrow S_1S_2} = \gamma_1\gamma_2, \quad (12a)$$

$$p_{\ell}^{I_1I_2 \rightarrow I_1S_2} = (1 - \gamma_1)\gamma_2, \quad (12b)$$

$$p_{\ell}^{I_1I_2 \rightarrow S_1I_2} = \gamma_1(1 - \gamma_2), \quad (12c)$$

$$p_{\ell}^{I_1I_2 \rightarrow I_1I_2} = 1 - \left[p_{\ell}^{I_1I_2 \rightarrow S_1S_2} + p_{\ell}^{I_1I_2 \rightarrow I_1S_2} + p_{\ell}^{I_1I_2 \rightarrow S_1I_2} \right]. \quad (12d)$$

IV. LOSS OPTIMIZATION PATTERNS

The machine learning problem we address is similar to a classification problem: For a given input, the model learns to assign it the correct label, i.e. the discrete state to which the node transition to. Contrary to standard classification problems, for a given input (μ, σ) , the label ν is not assigned deterministically, but

stochastically with LTP $p_{\sigma}^{\mu \rightarrow \nu}$, which from the classification point of view can be seen as a label distribution. This difference changes how the loss decreases during the learning phase. For example, when we consider a cross entropy objective function and deterministic labels, we expect the loss to descend gradually to zero because the entries of the label distributions are either zeros or ones, i.e. $p_{\sigma}^{\mu \rightarrow \nu} \in \{0, 1\}$. For stochastic labels, the model achieves maximal accuracy when the cross entropy is equal to the entropy of the label distribution, i.e. $H(p_{\sigma}^{\mu \rightarrow \nu})$. This is obtained by pointing out that minimizing the cross entropy with respect to the parameters Θ is completely equivalently to minimizing the Kullback-Liebler (KL) divergence between the ground truth $p_{\sigma}^{\mu \rightarrow \nu}$ and the model $\hat{p}_{\sigma}^{\mu \rightarrow \nu} = \hat{p}_{\sigma}^{\mu \rightarrow \nu}(\Theta)$ defined as follows:

$$\mathcal{D}(p_{\sigma}^{\mu \rightarrow \nu} || \hat{p}_{\sigma}^{\mu \rightarrow \nu}) = - \sum_{\nu \in \Omega} p_{\sigma}^{\mu \rightarrow \nu} \log \hat{p}_{\sigma}^{\mu \rightarrow \nu} - H(p_{\sigma}^{\mu \rightarrow \nu}). \quad (13)$$

Because the KL divergence is non-negative, it follows that its minimum value, corresponding to maximal accuracy, is exactly zero, hence

$$\min_{\Theta} \left[- \sum_{\nu \in \Omega} p_{\sigma}^{\mu \rightarrow \nu} \log \hat{p}_{\sigma}^{\mu \rightarrow \nu} \right] = H(p_{\sigma}^{\mu \rightarrow \nu}). \quad (14)$$

This motivates the monitoring of the entropy of the GNN predicted LTPs alongside the loss function during training. Indeed, because we expect $\hat{p}_{\sigma}^{\mu \rightarrow \nu} \approx p_{\sigma}^{\mu \rightarrow \nu}$ after a while, the entropy of the GNN predicted LTPs should be close to the true value of $H(p_{\sigma}^{\mu \rightarrow \nu})$, which in turn should remain of the same magnitude as the loss function if the training is going smoothly.

In Fig. 4, we show the evolution of different metrics throughout the training, namely the loss function, the GNN prediction entropy and the Jensen-Shannon distance (JSD) between the GNN predicted LTPs and the ones given by the maximum likelihood estimators (MLE). As expected, we see the loss decreasing as the training goes on, but does not descend to zero because of the stochasticity of the labels. In fact, it remains of the same order of magnitude as the GNN prediction entropy, as expected. However, the JSD clearly confirms that the model gets closer to the MLE, regardless of the fact that the loss is far from zero. Note that the JSD for the interacting contagion remains larger than the other contagion models because the MLE quality is quite poor in this case.

V. DATASET GENERATION

A. Algorithm

We generate data from each dynamics using the following algorithm:

1. Sample a graph G from a given generative model (e.g. the Erdős-Rényi or the Barabási-Albert models).

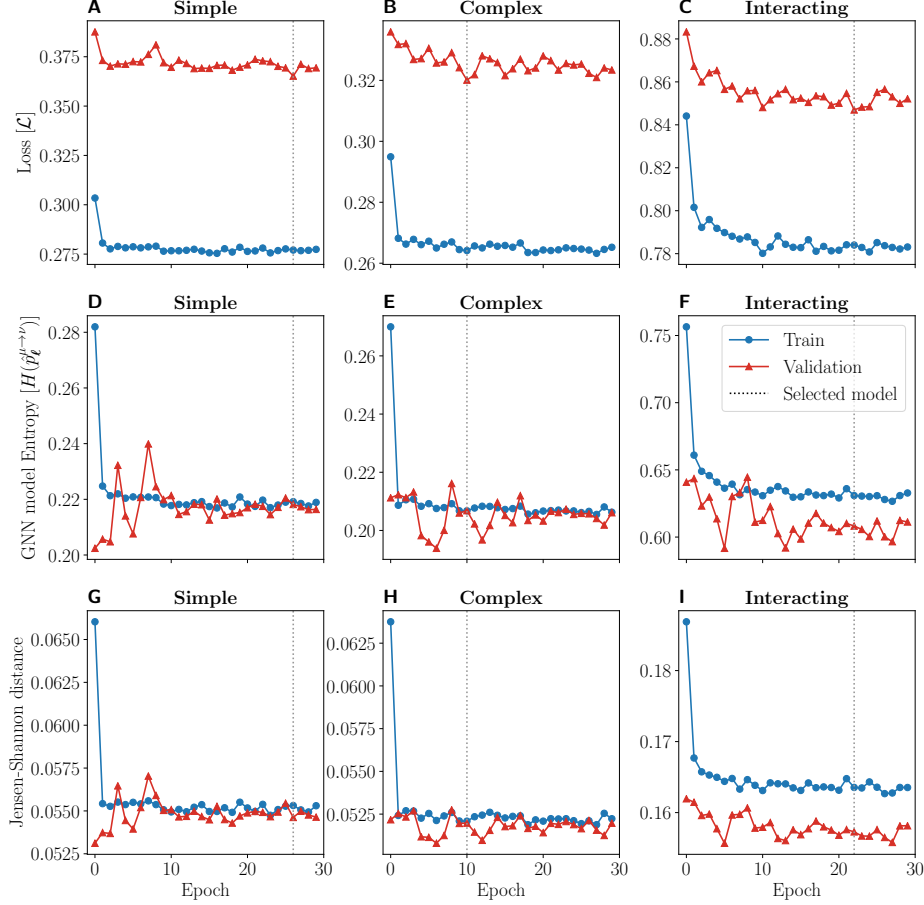


FIG. 4. **Loss optimization patterns during training.** (a–c) Loss as expressed by Eq. (3) in the main text, (d–f) average entropy of the GNN model predictions, (g–i) average Jensen-Shannon distance (JSD) between the GNN predicted LTPs and the ones given by the MLE. We show the results obtained when using Barabási-Albert networks to generate the data; similar conclusions are obtained when using data generated with Erdős-Rényi networks. All measures shown by these plots are approximated using the importance sampling strategies used to compute the loss. The vertical dotted lines show the minimum value of the validation loss, corresponding to the criterion for our model selection.

2. Initialize the state of the system $X(0) = (x_i(0))_{i=1..N}$. That is, for disease g , sample n_g uniformly between 0 and N and select uniformly and without replacement n_g nodes from the network. Then, assign a state to each node according to this selection: For instance, if node i is selected to have disease 1 and disease 2, it is assigned the state $I_1 I_2$.
3. At time t , sample $X(t + \Delta t)$ with the LTP conditioned on $X(t)$, where $\Delta t = 1$ without loss of generality. We record the states $X(t)$ and $X(t + \Delta t)$ for training as inputs and targets, respectively.
4. Repeat step 3 until $(t \bmod t_s) = 0$, where t_s denotes a resampling time. At this moment, apply

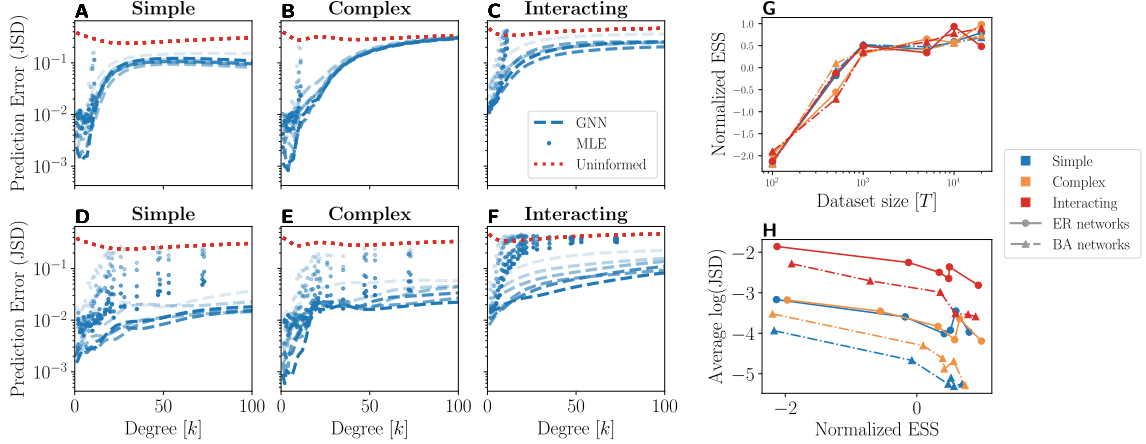


FIG. 5. (color online) **Impact of the dataset size on the prediction error.** (a–c) Models trained on ER networks, (d–f) models trained on BA networks, (g) normalized effective sample size (ESS), (h) average logarithm of the JSD error against the ESS. The specific dynamics are indicated on top of each column. We show the prediction error—calculated from the Jensen Shannon distance (JSD)—for different dataset size $T \in \{100, 500, 1000, 5000, 10000, 20000\}$. Solid lines correspond to the error of the GNN predictions, dotted lines denote the error of the uninformed baseline and symbols, the error of the MLE computed from the training dataset. On Figs. (a–f), the shade of blue indicates the value of T : darker blue means larger T . On Fig. (g–h), the colors indicate the type of dynamics used for training, and the lines and symbols, the type of networks. All hyperparameters are listed in Sec. IV.C of the Supplementary Material.

step 2 to reinitialize the states $X(t)$ and repeat step 3.

5. Stop when $t = T$, where T is the targeted number of samples.

The resampling step parametrized by t_s indirectly controls the diversity of the training dataset. We allow t_s to be small to emphasize on the performance of the GNN rather than the quality of the training dataset, while acknowledging that large values of t_s could lead to poor training. Because of the very nature of contagion dynamics, which contains absorbing and endemic steady states, it is expected that letting the dynamics evolve on its own could lead to datasets with high redundancy composed largely of degenerate states. This artificial mechanism has the advantage of increasing the effective sample size of the dataset by reducing this naturally occurring redundancy.

B. Impact of the Data Generation Hyperparameters

We investigate the impact of several hyperparameters involved in the data generation on the performance of the GNN, namely the dataset size T , the resampling time t_s and the number of nodes N . In general, we

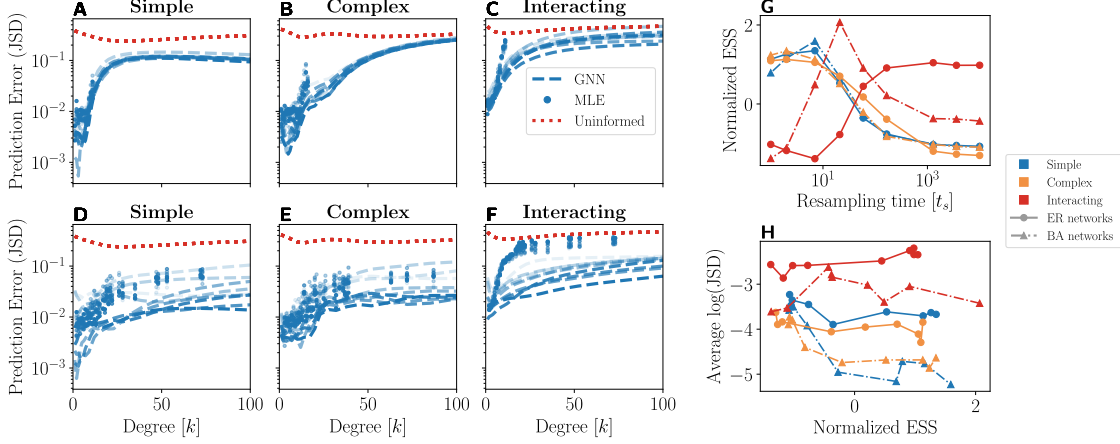


FIG. 6. (color online) **Impact of the resampling time on the prediction error.** (a–c) Models trained on ER networks, (d–f) models trained on BA networks, (g) normalized effective sample size (ESS), (h) average logarithm of the JSD error against the ESS. In these experiments, we fixed the resampling times to $t_s \in \{1, 2, 7, 21, 59, 166, 464, 1291, 3593, 10000\}$. For both the GNN and MLE errors, the shade of blue indicates the value of t_s : darker blue means smaller t_s . See the caption of Fig. 5 of the Supplementary Material for further details.

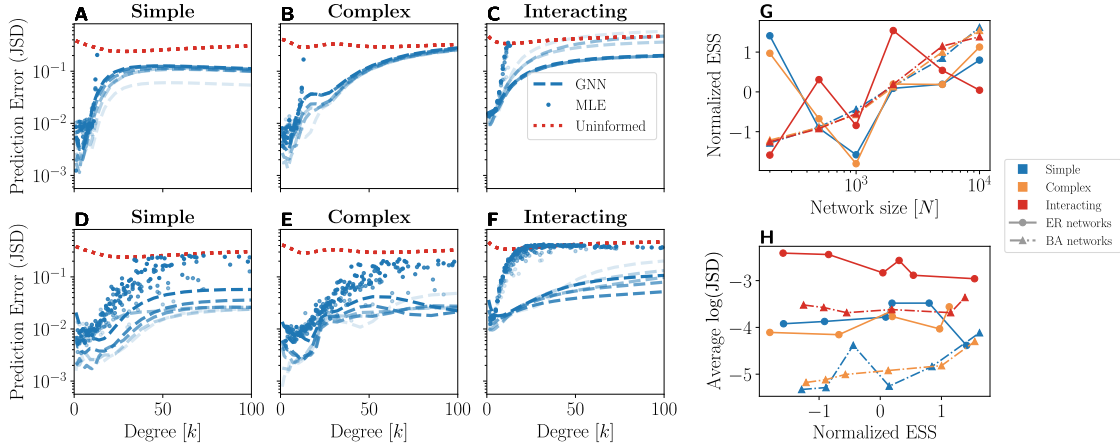


FIG. 7. (color online) **Impact of the number of nodes of training networks on the average error.** (a–c) Models trained on ER networks, (d–f) models trained on BA networks, (g) normalized effective sample size (ESS), (h) average logarithm of the JSD error against the ESS. In these experiments, we fixed the network sizes to $N \in \{200, 500, 1000, 5000, 10000\}$. In order to better appreciate the impact of increasing N , we fixed $T = 10^7/N$ to maintain a comparable number of samples, and fixed $\langle k \rangle = 4$ in all experiments. For both the GNN and MLE errors, the shade of blue indicates the value of N : darker blue means larger N . See the caption of Fig. 5 of the Supplementary Material for further details.

expect the performance to increase with the variety of the dataset. To quantify this variety, we use the effective sample size (ESS), given by

$$n_{\text{eff}} = \frac{\left(\sum_{\mu, \ell} n_{\ell}^{\mu}\right)^2}{\sum_{\mu, \ell} \left(n_{\ell}^{\mu}\right)^2} \quad (15)$$

where

$$n_{\ell}^{\mu} = \sum_{t=1}^T \sum_{i \in \mathcal{V}} I[x_i(t) = \mu] I[\ell_i(t) = \ell], \quad \ell_i(t) = (\ell_i^{\mu}(t))_{\mu \in \Omega} = \left(\sum_{j \in \mathcal{N}_i} I[x_j(t) = \mu] \right)_{\mu \in \Omega}. \quad (16)$$

where $I[c]$ is an indicator function where $I[c] = 1$ if c is true, and $I[c] = 0$ otherwise. We expect that larger ESS will lead to a better approximated loss, in turn yielding better trained models. To compare all experiments, we consider the normalized ESS, denoted by

$$\frac{n_{\text{eff}} - \mathbb{E}(n_{\text{eff}})}{\sqrt{\text{var}(n_{\text{eff}})}} \quad (17)$$

where the expectation and the variance are taken over the values of hyperparameters.

On Figs. 5-6-7, we show the prediction error, measured by the JSD, on star graphs while changing the different data generation hyperparameters (T , t_s and N , respectively). As we can see from Figs. 5-6, increasing T and reducing t_s tend to help the models achieve higher performance, with diminished prediction errors. In most cases, this is well correlated with the ESS which tend to be large when the error is small, while the effect is more subtle for the resampling time than for the dataset size. It is interesting to note that small values of t_s are not always ideal, as we observe increase in ESS for the interacting contagion dynamics when t_s is larger.

Surprisingly, increasing the network size N does not seem to increase the performance of our models. First, for ER networks, increasing N does not tend to increase the ESS. This is expected because the maximum degree only slightly increase when the number of nodes is increased, for fixed the average degree $\langle k \rangle$. Hence, we do not observe additional degree classes when N is marginally increased and the training dataset variety remains similar. For BA networks, we observe something different: While the increase in N leads to higher ESS, there is still no substantial gain in performance. This can be explained by looking at the degree distribution. As more nodes are added to the network, the degree classes get more populated, resulting in increased ESS. However, because the degree distribution is scale-free (with exponent -3), these are not populated evenly and more degree classes are created as N increases. This has the effect of raising the problem difficulty, because increasing the number of accessible degree classes also increases the number of cases—LTPs with specific inputs—the GNN model needs to fit.

VI. TRAINING SETTINGS

A. Optimization

We use the Rectified Adam optimization algorithm presented in Ref. [6]. Similarly to Ref. [7], this algorithm minimizes an objective function by estimating the average and variance of its gradient from moving averages. These moving averages are parametrized by $b_1, b_2 \in [0, 1)$ for the average and the variance respectively, which we specify below.

B. Validation Dataset Selection

Validating the model is a crucial step of the learning pipeline where the performance of the model is objectively evaluated. In most cases, it is done by selecting a subset of the training dataset, called the validation dataset, from which the model will not learn from. The performance is then evaluated by computing the average loss with respect to this validation dataset, which allows us to monitor the learning process.

The selection of the validation set is usually done by sampling randomly a small percentage, about 20%, of samples in the training dataset. In general, this is not an issue in high dimensional problems where each data point is virtually unique. However, in our case, the data points correspond to each individual input (μ, σ) , which is likely to be repeated multiple times. Therefore, it is not recommended to proceed by splitting the training dataset at random. In fact, this could jeopardize the whole validation procedure if the training and validation datasets distribution are too similar.

Instead, we propose to sample the transitions by importance similarly to the importance sampling scheme approximating the loss function presented in the main text. Let us consider $\mathcal{W}(t) \subset \mathcal{V}$, a subset of nodes at time t selected for validation. The probability that the transition of node i at time t belongs to the validation dataset is equal to

$$\Pr [i \in \mathcal{W}(t)] = \frac{\rho(x_i(t), \ell_i(t))^{-\delta}}{\sum_{i \in \mathcal{V}} \rho(x_i(t), \ell_i(t))^{-\delta}} \quad (18)$$

where $\rho(\mu, \ell)$ denotes the input distribution, and $\delta \geq 1$ is a parameter controlling the bias towards rare inputs. During training, the loss function is then approximated by

$$\mathcal{L}(\Theta) \simeq \sum_{t \in \mathcal{T}'} \sum_{i \in \mathcal{V}'(t)} \frac{\omega_i(t)}{|\mathcal{T}'| |\mathcal{V}'(t)|} \left[-\log \hat{p}_{x_{\mathcal{N}_i}(t)}^{x_i(t) \rightarrow x_i(t+\Delta t)} \right] \quad (19)$$

where $\mathcal{V}'(t) = \mathcal{V} \setminus \mathcal{W}(t)$. Sampling the validation dataset by importance allows us to validate the model on all available inputs with equal weights, i.e. when $\delta \rightarrow 1$. It also helps to minimize the similarity between the training and the validation datasets, as the rarest inputs will be likely only be available in the latter.

C. Hyperparameters

For all experiments, we fix the optimizer parameters to $b_1 = 0.9$ and $b_2 = 0.999$ as was suggested in Ref. [7] and we schedule the learning rate ϵ to reduce by a factor 2 every 10 epochs, that is $\epsilon_{i+1} = 2^{\lfloor \frac{i \bmod 10}{10} \rfloor} \epsilon_i$ with initial value $\epsilon_0 = 0.0005$. A weight decay of 10^{-4} is used as well to help regularize the training. We set the number of epochs to 20 and choose the model with the lowest loss on validation datasets as our best model. We fix the importance sampling bias exponents for the training and the validation to $\lambda = 0.6$ and $\delta = 0.8$, respectively. For the data generation, we fix the sequence size $t_s = 2$ and we used $T = 10000$ samples for the experiments presented in the main paper.

VII. MEAN FIELD FRAMEWORK

A. Approximate master equations

The mean field framework we use is inspired by [8] and provides an approximate solution to the stationary distribution of contagion dynamics using a set of discrete-time approximate master equations (AME). To construct the AME, we consider a set of LTPs $p_\ell^{\mu \rightarrow \nu}$ and a state matrix $\mathbf{Q}(t)$, where the entry $[\mathbf{Q}(t)]_{\mu,k}$ corresponds to the probability that a node of degree k is in state μ at time t . Then, the AME that describes the evolution of $\mathbf{Q}(t)$ is expressed as follows:

$$[\mathbf{Q}(t + \Delta t)]_{\mu,k} = \sum_{\nu} [\mathbf{Q}(t)]_{\nu,k} \sum_{|\ell|=k} M_k(\ell; t) p_\ell^{\mu \rightarrow \nu} \quad (20)$$

where $M_k(\ell)$ is the probability that the neighborhood of a node of degree k has state ℓ at time t , recalling that $[\ell]_\mu = \ell^\mu$ corresponds to the number of neighbors in state μ . The probability $M_k(\ell)$ is approximated by a multinomial distribution,

$$M_k(\ell; t) = k! \prod_{\nu} \frac{\phi^\nu(t)^{\ell^\nu}}{\ell^\nu!} \quad (21)$$

where $\phi^\nu(t)$ is the probability that a node at the end of a randomly selected edge is in state ν at time t . The underlying assumption behind this parameterization of $M_k(\ell)$ is that the neighbors of a given node are assumed dynamically and structurally uncorrelated. These assumptions lead us to the following closed form for $\phi^\nu(t)$:

$$\phi^\nu(t) = \frac{\sum_k k \rho_k [\mathbf{Q}(t)]_{\nu,k}}{\langle k \rangle} \quad (22)$$

where $\rho_k = \Pr(K = k)$ is the probability that a node has degree k and $\frac{k \rho_k}{\langle k \rangle}$ is the probability to reach a node of degree k from a randomly selected edge.

We use this mean field framework to compute the stationary distributions of the three contagion dynamics we investigated in the main text, as well as the stationary distributions predicted by the trained GNN models. To simplify our analysis, we consider that $\rho_k = e^{-\kappa} \kappa^k / k!$ is a Poisson distribution with parameter and κ with a truncated support $\mathcal{K} = [k_{\min}, k_{\max}] \subset \mathbb{Z}^+$. In our experiments, we consider that the average degree $\langle k \rangle$ is our control parameter, rather than κ . Therefore, to ensure that $\langle k \rangle$ remains fixed, we fix the support using

$$k_{\min} = \max \left\{ 0, \lfloor \langle k \rangle \rfloor - 7 \right\}, \quad k_{\max} = \max \left\{ 14, \lceil \langle k \rangle \rceil + 7 \right\} \quad (23)$$

where the operations $\lfloor \cdot \rfloor$ and $\lceil \cdot \rceil$ are the floor and ceil functions, respectively. This guarantees that $|\mathcal{K}| = k_{\max} - k_{\min} + 1 = 15$. Then, we fix κ by solving numerically the following equation:

$$\sum_{k \in \mathcal{K}} k \rho_k = \sum_{k \in \mathcal{K}} k \frac{e^{-\kappa} \kappa^k}{k!} = \langle k \rangle. \quad (24)$$

To apply the AME framework to a GNN model, we begin by extracting its LTPs beforehand using the prescription described in the main text involving the star graph of $k + 1$ nodes, whose central node can generate any desired input (μ, ℓ) given its degree k . Then, Eq. (20) is solved numerically using a relaxation method [9].

It is possible to obtain a more refined version of Eq. (20), as prescribed in Ref. [8]. However, even in this simple case, iterating Eq. (20) becomes rapidly tedious as the number of available states increases. Specifically, to update Eq. (20), one needs to enumerate

$$|\Omega| \binom{k + |\Omega| - 1}{|\Omega| - 1} \quad (25)$$

terms, which scales poorly with $|\Omega|$ and k . The scaling is even worst for more refined frameworks.

B. Numerical Evaluation of the Thresholds

Contagion dynamics are known to have phase transitions which delineate different dynamical behaviors. More specifically, beyond some threshold values of the dynamical and structural parameters, contagion dynamics shift abruptly from an absorbing phase, where all nodes are susceptible in the steady state—denoted \mathbf{Q}^* where $[\mathbf{Q}^*]_{\mu,k} = I[\mu = S]$ —, to an endemic phase in which a nonzero fraction of nodes remains infected over time [10–12]. We note the endemic state \mathbf{Q}^\dagger , where $[\mathbf{Q}^\dagger]_{\mu,k} > 0$ is obtained numerically from Eq. (20) using a relaxation method with the initial condition $[\mathbf{Q}(0)]_{\mu,k} = (1 - \epsilon)I[\mu \neq S] + \epsilon I[\mu = S]$ assuming $\epsilon \ll 1$ [13]. In the case of the susceptible-infected-susceptible dynamics (SIS), the phase transition occurs at the point where the infection and recovery probabilities, τ and γ , are related to the first

and second moments of the degree distribution as follows:

$$\frac{\tau}{\gamma} = \frac{\langle k \rangle}{\langle k^2 \rangle}. \quad (26)$$

One obtains this relation by computing the stability $\lambda(\mathbf{Q}^*)$ of the absorbing state \mathbf{Q}^* , which corresponds to the largest eigenvalue of the Jacobian matrix $\mathbf{J}(\mathbf{Q}^*)$ evaluated at that point. The entries of the Jacobian matrix, indexed by the pairs (μ, k) and (μ', k') , evaluated at an arbitrary point \mathbf{Q} are computed as follows:

$$[\mathbf{J}(\mathbf{Q})]_{(\mu,k),(\mu',k')} = \left. \frac{\partial[\mathbf{Q}(t + \Delta t)]_{\mu,k}}{\partial[\mathbf{Q}(t)]_{\mu',k'}} \right|_{\mathbf{Q}(t)=\mathbf{Q}}. \quad (27)$$

A fixed point \mathbf{Q} is stable when $\lambda(\mathbf{Q}) < 1$, and unstable otherwise. As we consider that the parameters of contagion dynamics to remain unchanged, we compute the thresholds of the phase transitions with respect to the average degree $\langle k \rangle$. For simple contagion dynamics, the threshold is obtained numerically by solving for the value of $\langle k \rangle$ for which the stability of the absorbing state yields $\lambda(\mathbf{Q}^*) = 1$. For complex and interacting dynamics, we must find two thresholds that delineate a bistable regime where both the absorbing state \mathbf{Q}^* and the endemic state \mathbf{Q}^\dagger are stable. Therefore, we apply the same strategy and solve numerically for $\langle k \rangle$ the two equations $\lambda(\mathbf{Q}^*) = 1$ and $\lambda(\mathbf{Q}^\dagger) = 1$.

-
- [1] P. Veličković, G. Cucurull, A. Casanova, A. Romero, P. Liò, and Y. Bengio, “Graph attention networks,” in *International Conference on Learning Representations* (2018).
- [2] W. L. Hamilton, R. Ying, and J. Leskovec, “Representation Learning on Graphs: Methods and Applications,” (2017), [arXiv:1709.05584](https://arxiv.org/abs/1709.05584).
- [3] L. Isella, J. Stehlé, A. Barrat, C. Cattuto, J.-F. Pinton, and W. Van den Broeck, “What’s in a crowd? Analysis of face-to-face behavioral networks,” *J. Theor. Biol.* **271**, 166–180 (2011).
- [4] M. Génois and A. Barrat, “Can co-location be used as a proxy for face-to-face contacts?” *EPJ Data Sci.* **7**, 11 (2018).
- [5] R. Mastrandrea, J. Fournet, and A. Barrat, “Contact Patterns in a High School: A Comparison between Data Collected Using Wearable Sensors, Contact Diaries and Friendship Surveys,” *PLOS ONE* **10**, e0136497 (2015).
- [6] L. Liu, H. Jiang, P. He, W. Chen, X. Liu, J. Gao, and J. Han, “On the Variance of the Adaptive Learning Rate and Beyond,” [arXiv , 1908.03265](https://arxiv.org/abs/1908.03265) (2020).
- [7] D. P. Kingma and J. Ba, “Adam: A Method for Stochastic Optimization,” (2014), [arXiv:1412.6980](https://arxiv.org/abs/1412.6980).
- [8] P. G. Fennell and J. P. Gleeson, “Multistate Dynamical Processes on Networks: Analysis through Degree-Based Approximation Frameworks,” *SIAM Rev.* **61**, 92–118 (2019).
- [9] W. H. Press, S. A. Teukolsky, W. T. Vetterling, and B. P. Flannery, *Numerical Recipes 3rd Edition: The Art of Scientific Computing*, 3rd ed. (Cambridge University Press, USA, 2007).
- [10] I. Z. Kiss, J. C. Miller, and P. L. Simon, *Mathematics of Epidemics on Networks* (Springer, 2017) p. 598.

- [11] R. Pastor-Satorras, C. Castellano, P. Van Mieghem, and A. Vespignani, “Epidemic processes in complex networks,” [Rev. Mod. Phys. **87**, 925–979 \(2015\)](#).
- [12] J. Sanz, C.-Y. Xia, S. Meloni, and Y. Moreno, “Dynamics of Interacting Diseases,” [Phys. Rev. X **4**, 041005 \(2014\)](#).
- [13] Equivalently, in the case of the interacting contagion dynamics, we use $[Q(0)]_{\mu,k} = (1 - \frac{\epsilon}{4})I[\mu \neq S_1 S_2] + \epsilon I[\mu = S_1 S_2]$ as an initial condition.